Atmospheric response to zonal variations in mid-latitude SST: Transient and stationary eddies and their feedback*

Masaru Inatsu

Graduated School of Environmental Earth Science, Hokkaido University, Sapporo, Japan

Hitoshi Mukougawa

Disaster Prevention Research Institute, Kyoto University, Uji, Kyoto, Japan

Shang-Ping Xie

International Pacific Research Center and Department of Meteorology, University of Hawaii, Honolulu, Hawaii.

(Manuscript submitted on 18 October 2002, in a final form on 25 April 2003, to Journal of Climate)

---

*This is IPRC contribution # xxx and SOEST contribution # yyyy.

Corresponding author address: Dr. Masaru Inatsu, Graduate school of Environmental Earth Science, Hokkaido University, N10W5, Kita, Sappoto, Hokkaido, 0600810, Japan.

E-mail: inaz@ees.hokudai.ac.jp

Abstract

We have investigated midwinter storm track response to zonal variations in mid-latitude sea surface temperatures (SSTs) using an atmospheric general circulation model under aqua-planet and perpetual January conditions. Zonal wavenumber-one SST variations with a meridionally confined structure are placed at various latitudes. Having these SST variations centered at 30°N leads to a zonally localized storm track, while the storm track becomes nearly zonally uniform when the same SST forcing is moved further north at 40°N and 50°N. Large (Small) baroclinic energy conversion north of the warm (cold) SST anomaly near the axis of storm track (near 40°N) is responsible for the large (small) storm growth. The equatorward transfer of eddy kinetic energy by the ageostrophic motion and the mechanical damping are important to diminish the storm track activity in the zonal direction.

Significant stationary eddies form in the upper troposphere, with a ridge (trough) northeast of the warm (cold) SST anomaly at 30°N. Heat and vorticity budget analyses indicate that zonally localized condensational heating in the storm track is the major cause for these stationary eddies, which in turn exert a positive feedback to maintain the localized storm track by strengthening the vertical shear near the surface. These results indicate an active role of synoptic eddies in inducing deep, tropospheric-scale response to mid-latitude SST variations. Finally, the application of the model results to the real atmosphere is discussed.

1. Introduction

The Northern Hemisphere (NH) wintertime circulation displays pronounced zonal variations due to terrestrial surface conditions such as topography, land-sea heat distribution, and sea surface temperature (SST). Climatological stationary waves have been studied with various models ranging from atmospheric general circulation models (AGCMs; *e.g.*, Manabe and Terpstra 1974) to linear models (*e.g.*, Valdes and Hoskins 1989). Planetary-scale extratropical stationary eddies with zonal wavenumbers two or three are forced by large-scale orography like the Himalayas and the Rockies (Held 1983) and basin-scale variation in tropical SST (*e.g.*, Simmons 1982; Inatsu et al. 2002a). Synoptic-scale transient eddies in the NH, on the other hand, are found to be concentrated in certain longitudinal bands called storm tracks that are located just downstream of the strong westerly jet south to the stationary trough where the vertical shear and hence baroclinicity are large in the lower troposphere above the planetary boundary layer (PBL; Hoskins and Valdes 1990).

Fig. 1.

The Southern Hemisphere (SH) wintertime tropospheric circulation shows weak but significant zonal variations (Fig. 1). Contrary to what is observed in the NH, the SH winter (July) storm track is located upstream of the subtropical jet core in the upper troposphere (Figs. 1b and 1c). Based on correlation analyses in space and time, Nakamura and Shimpo (2002; hereafter NS) show that the SH storm track is controlled by the near-surface Eady (1949) growth rate, called baroclinicity (Lindzen and Farrell 1980) defined as,

$$\sigma_{\rm BC} = 0.31\, f \left| \frac{\partial \boldsymbol{v}}{\partial z} \right| / \mathcal{N}, \tag{1}$$

where f is the Coriolis parameter, $\boldsymbol{v} = (u, v)$ is the horizontal wind velocity, and $\mathcal{N}$ is

the Brunt Väisälä frequency. NS suggest that in the SH winter, near-surface baroclinicity distribution may be largely determined by meridional SST gradient (Fig. 1a).

A recent study of Inatsu et al. (2002b; hereafter IMX) hints at a mid-latitude SST control of the storm track that seems consistent with NS's observations of the SH storm track. In an experiment using aqua-planet conditions where a zonal wavenumber one (WN-1) SST distribution is imposed in the model mid-latitudes, the storm track is found over and downstream of the meridional SST gradient maximum, despite weak stationary eddies in the upper troposphere. Taken together, IMX and NS's results suggest that zonal variations in mid-latitude SST are an important factor modulating the SH storm activity. The SH is nearly water covered and close to the aqua-planet conditions IMX use. In the NH, since oceans are divided into smaller basin, major orographic features play a major role in the dynamics of both stationary and transient eddies.

A related issue is how the atmosphere reacts to changes in the mid-latitude SST, which is subject to large uncertainties and a stumbling block in understanding and simulating off-equatorial climate variability. In the extratropics, the atmospheric effect on SST is well established but AGCMs disagree strongly on their response to SST changes both in spatial pattern and magnitude (Robinson 2000; Kushnir et al. 2002). Among other difficulties, AGCM response is highly sensitive to slight changes in the basic state, varying drastically from one winter month to another (Kushnir and Held 1996; Peng et al. 1997). There are confusing and sometimes mutually contradictory results even in the studies of the stationary-eddy response to mid-latitude SST anomalies (Robinson 2000). IMX's result suggests that extratropical SST anomalies may exert a more robust effect on the storm

track than on the stationary eddies.

The purpose of this study is to further investigate the atmospheric response to mid-latitude SST variations by using an AGCM. While IMX demonstrated a robust storm-track response to mid-latitude SST variations, a number of important issues remain to be addressed. First, based on our brief review in the above, it is quite possible that the model response is sensitive to where SST variations are placed. This sensitivity will be explored here. Second, we will perform a number of diagnoses to establish the chain of reactions to SST changes and understand the mechanism for maintaining the storm track. For example, is the SST effect on near-surface baroclinicity important for the storm growth, and what terminates a storm track? Finally, we explore the feedback of transient eddies onto the time-mean circulation. Our results show that the enhanced baroclinic conversion over the high baroclinic zone near the surface is indeed the main cause of zonal variations in synoptic eddy activity. This storm track response further leads to significant stationary eddies in the upper troposphere.

To simplify the experimentation and analysis, we run the AGCM under aqua-planet and perpetual-January conditions. The mid-latitude SST variations have a zonal WN-1 structure, while the tropical SST is set zonally uniform. Without the complication of orography and continents, the aqua-planet design seems to be the minimum AGCM system to investigate the complicated dynamics of atmospheric response to changing SST in the mid-latitudes. Although not directly applicable to NH climate, the results from our aqua-planet runs are probably a useful stepping stone for understanding the SST modulation of mid-latitude SH climate. An improved understanding from this exercise will help design

and interpret more realistic experiments.

The rest of the paper is organized as follows. Section 2 describes the model and experimental designs. Section 3 examines the sensitivity of the model response to the latitudinal position of imposed SST anomalies. By diagnosing model output, sections 4 and 5 study the mechanism for storm track and stationary eddy response, respectively. Section 6 discusses implications for current research in extratropical climate. Section 7 is a summary.

2. Model and experiments

We use an AGCM developed at Center for Climate System Research (CCSR) of University of Tokyo and National Institute for Environmental Studies (NIES). It is a community model for Japanese universities and used at several national research institutes in Japan. It is based upon the primitive equations on the sphere and includes parameterization of physical processes such as radiation (Nakajima and Tanaka 1988), cumulus convection (Arakawa and Schubert 1974), large-scale cloud condensation (Le Treut and Li 1991), turbulent mixing (Mellor and Yamada 1982), gravity wave drag (McFarlane 1987), surface flux (Louis 1979), and ground hydrology. See Numaguti et al. (1997) and Numaguti (1999) for more detail. A version of triangular truncation at the total wavenumber 42 (T42) with 20 sigma levels (L20) in the vertical is used in order to resolve the synoptic-scale eddies. Each run lasts for 1500 days after a spinup period to obtain stable statistics. The control run with 1500 days integration of the model reasonably reproduces the observed mean circulation and the storm tracks (Inatsu et al. 2002a).

We have conducted all the experiments under the perpetual January condition where the

insolation at its January-mean distribution is fixed, and under the aqua-planet condition where the model surface is covered by water over the whole globe. A SST distribution is given by,

$$T_o(\lambda,\phi) = \begin{cases} 301.15 - 32.0\sin^2(\phi - 8°\mathrm{S}) + \\ \quad 2.5\ \sin\lambda\ \exp\left[-\dfrac{(\phi-\phi_0)^2}{200}\right], \\ \qquad\qquad \text{for } T_o > 271.4, \\ 271.4 \qquad\qquad \text{elsewhere}, \end{cases} \tag{2}$$

where λ and ϕ denote longitude and latitude measured by degree, respectively. In the tropics and the SH, SST is zonally uniform with the meridional maximum at 8°S. Thus, the NH is in a winter condition on this aqua-planet. We impose SST variations of a WN-1 structure in the zonal and a Gaussian structure in the meridional direction with a central latitude at ϕ_0 and the e-folding scale of 14°. The amplitude of SST forcing is 2.5 K, somewhat larger than observation, to ensure a prominent model response.

Fig. 2.

We carry out three experiments with $\phi_0 = 30°$N, 40°N, and 50°N in Eq. (2), which are referred to as M30, M40, and M50, respectively. Figure 2 shows the SST distributions used in three runs. As reference of these experiments, the aqua-planet control run named CTR is also conducted with no land and SST given by the zonal average of Eq. (2).

3. Sensitivity to the latitude of SST forcing

This section examines stationary eddies and synoptic-scale eddy activity in three aqua-planet AGCM experiments to investigate the dependence on the latitudinal position of mid-latitude SST forcing. Here the term "anomaly" refers to the departure from the zonal

mean.

a. Spatial distribution

Fig. 3.

Figure 3 shows zonal-mean zonal wind velocity as a function of latitude and pressure, which exhibits similar gross features to observations in both hemispheres, except for a too strong subtropical jet. The difference from CTR (shading in Fig. 3) is quite large north of 45°N in the M30 run, presumably because of changes in momentum flux by transient eddies. In both M40 and M50, zonal wind speed difference from CTR is positive around 20°N and negative around 40°N, because convergence of momentum flux around 40°N and 300 hPa is reduced (not shown). The zonal-mean response to zonal variations of mid-latitude SST is very small in the lower troposphere. In the following, we focus on the zonally asymmetric response.

Fig. 4.

Figure 4a shows the geopotential height anomaly at 250 hPa for M30. The shading in Fig. 4a denotes the region where the statistical significance of the anomaly exceeds 95% based on a test procedure described in Appendix A. Stationary eddies have a dominant WN-1 structure in the zonal direction and are statistically significant in the 20°N–50°N band, with an amplitude maximum of 70 m. A sizable stationary anticyclone (cyclone) is located northeast of the warm (cold) SST anomaly, leading to a local maximum in the wind speed of the subtropical jet at 45°W and 30°N. Synoptic-scale eddy activity, represented by root-mean-square variance of 2.5–6-day bandpass filtered geopotential height (Blackmon 1976), shows pronounced zonal variations with a maximum of 70 m and a minimum of 50 m northeast of the warm and cold SST anomalies, respectively. Anomalies of synoptic-scale

eddy activity (shade in Fig. 4b) are large and statistically significant in the extratropics north of 35°N.

Stationary eddies become weaker as the SST anomalies are shifted to the north, but maintain a similar zonal phase relation with the underlying SST variations. The maximum height anomalies are centered at 50°N in both M40 and M50, but they are very weak and statistically insignificant in M50 (Figs. 4c and 4e). The storm track in both runs becomes nearly zonally uniform (Figs. 4d and 4f), and its zonal variation also becomes insignificant.

Fig. 5.

In the lower atmosphere at 850 hPa (Fig. 5), significant stationary eddies are centered at 60°N in M30, with a trough (ridge) northeast of the warm (cold) SST patch. This leads to the acceleration of westerlies over or north of the positive SST anomalies. As an index of storm activity, we use the lower tropospheric northward heat flux by transient eddies with periods less than 10 days, which tends to track growing baroclinic waves. There are pronounced zonal variations in this index in M30, with a maximum north of the SST anomaly maximum. In M40 and M50, zonal variations in both stationary and transient eddies are much weaker as in the upper troposphere. In M50, a weak maximum of the transient eddy activity takes place south of the cold SST anomaly center both at 250 and 850 hPa.

Fig. 6.

Figure 6 shows the longitude-pressure cross sections of stationary eddies and storm activity along 40°N, the latitude where the axis of the storm track is located. In M30 and M40, stationary eddies are tilted westward with height above the PBL. In particular, a baroclinic structure of stationary eddies is prominent over the warm SST anomaly in M30 and M40: stationary cyclonic eddies reside near the surface which anticyclonic eddies

exist in the upper troposphere. The amplitude of the anomaly increases rapidly in the PBL over the SST anomaly center. Stationary eddies are insignificant in M50. In M30, the storm track is strongly localized throughout the troposphere (Fig. 6b). The local maximum of storm activity in the upper troposphere shifts slightly to the east of that in the lower troposphere. In both M40 and M50, synoptic-scale eddy activity is more or less zonally symmetric in the troposphere (Figs. 6d and 6f).

b. Surface control of storm track variations

In the M30 experiment, the storm activity is enhanced at 100°E and 40°N where the mid-latitude ridge exists, and is suppressed at 60°W and 40°N where the mid-latitude trough exists (Fig. 4). This is consistent with IMX's result that variations in the mid-latitude SST gradient force a zonally localized storm track with baroclinicity in PBL modulating the storm activity in their aqua-planet model without land, orography and tropical forcing.

Fig. 7.

Meridional SST gradient contributes directly to baroclinicity through the thermal wind relation. North (south) of the positive SST anomaly center, the vertical shear of the westerly is large (small). This seems to explain the gross features of the vertical shear anomaly distribution at 900 hPa in the M30 run (Figs. 7a and 7b)[1]. Figure 7 displays the time-mean distributions of vertical wind shear anomaly at 900 hPa derived from the AGCM and inferred from the prescribed SST using the thermal wind relation: $\left(\frac{\partial u}{\partial p}\right)^* = -\frac{R}{fp}\left(\frac{\partial T}{\partial y}\right)^*$ where T is temperature, p is pressure, and R is the gas constant. We here assume that

[1]Hoskins and Valdes (1990) showed that 780-hPa baroclinicity [Eq. (1)] is well correlated with the storm activity in the NH winter, but in our model, the 780-hPa baroclinicity is nearly zonally uniform along 40°N. Instead, near-surface baroclinicity seems to support the growth of transient eddies.

pressure is given as 900 hPa and temperature at 900 hPa is equal to SST given by Eq. (2). We subtract the zonal-mean field because vertical wind shear inferred from the SST distribution is dominated by the latitudinal dependence of f and increases equatorward, while maximum vertical wind shear is found at 37°N near the axis of maximum storm activity (Fig. 3a). In M30 along 40°N, the zonal variation in AGCM vertical shear is three times of that inferred from SST. In M50, by contrast, the AGCM shear is almost zonally uniform along 40°N, although zonal variation in SST-inferred shear is the same as that in M30. SST gradient is thus not the only factor that controls baroclinicity along the axis of storm track. As will be shown in section 5, stationary eddies and their interaction with the storm track are important for maintaining the vertical shear and baroclinicity near 40°N.

Fig. 8.

Latent heat release due to precipitation plays an important role in the extratropical storm growth (Gutowski et al. 1992). SST, via its effect on the surface latent heat release, can influence precipitation and hence the storm track. In the M30 run, rainfall displays strong zonal variations with the maximum around 70°E and 40°N (Fig. 8d), as a result of surface evaporation that closely follows the SST distribution (Fig. 8b) as well as poleward moisture flux by transient and stationary eddies (Fig. 8c). By contrast, sensible heat flux is one order of magnitude smaller and secondary (Fig. 8a).

We hypothesize that the combined SST effects on vertical wind shear and precipitation is possibly a key to forming stationary eddies and further enhancing storm activity (Fig. 4). In the M30 run, the increase in westerly shear and precipitation north of the positive SST anomaly center both act to intensify the growth of storms there, resulting in a distinct localized storm track. In the M50 run, by contrast, these two SST effects oppose each

other, giving rise to a rather zonally uniform storm track. A closer look into Figs. 4 and 5 indicates a marginally significant maximum in storm activity south of the negative SST anomaly center (90°W), suggesting that the SST gradient effect exceeds slightly the precipitation effect.

In the rest of the paper, we present several diagnostic analyses to support the hypothesis of surface control of storm activity and explore possible feedbacks that the storm track might have on stationary eddies. We focus on the M30 run since it shows strong zonal variations in both the time-mean flow and storm activity. After these diagnoses, we will move our attention to the application to the real atmosphere.

4. Storm track formation

In this section, we analyze the generation and dissipation mechanism of the eddy kinetic energy (EKE) to understand the most important agent to localize the storm track in the zonal direction. Here, high-frequency transient fluctuations are defined as the variation with periods less than 10 days. We will start with the momentum equation,

$$\left(\frac{\partial}{\partial t} + \boldsymbol{u}\cdot\nabla\right)\boldsymbol{v} + f\boldsymbol{k}\times\boldsymbol{v} = -\nabla_{\mathrm{H}}\Phi + \boldsymbol{X}, \tag{3}$$

where ω is vertical velocity, $\boldsymbol{u} = (u, v, \omega)$, ∇ and ∇_{H} are three and two dimensional differential operator, respectively, Φ is geopotential height, and $\boldsymbol{X}$ represents the dissipation. Taking the inner product of high-frequency horizontal wind vector with the equation for high-frequency eddies (prime) embedded in the time-mean field (overbar) derived from Eq. (3), we obtain the following equation for high-frequency EKE by carrying out the time

average and the vertical integration from 900 hPa to 125 hPa ($\| \bullet \|$),

$$\left\| \frac{\partial \mathcal{K}_e}{\partial t} \right\| = \underbrace{\left\| -\frac{R}{p}\,\overline{\omega' T'} \right\|}_{\text{(a)}} + \underbrace{\left\| -\nabla_{\mathrm{H}} \cdot \left(\overline{\boldsymbol{v}' \Phi'}\right) \right\|}_{\text{(b)}} +$$
$$\underbrace{\left\| \overline{\mathcal{R}} \right\|}_{\text{(c)}} + \underbrace{\left\| -\overline{\boldsymbol{v}} \cdot \nabla_{\mathrm{H}} \mathcal{K}_e \right\|}_{\text{(d)}} +$$
$$\underbrace{\left\| -\left[\overline{u'^2}\,\frac{\partial \overline{u}}{\partial x} + \overline{u'v'}\left(\frac{\partial \overline{u}}{\partial y} + \frac{\partial \overline{v}}{\partial x}\right) + \overline{v'^2}\,\frac{\partial \overline{v}}{\partial y}\right] \right\|}_{\text{(e)}}, \tag{4}$$

where $\mathcal{K}_e = \frac{1}{2}\left(\overline{u'^2} + \overline{v'^2}\right)$, and $\mathcal{R}$ is mechanical damping of EKE mainly due to surface friction, which is estimated by the residual in Eq. (4). Here we neglect both the vertical geopotential flux divergence at the upper and the lower boundaries, the vertical advection of EKE by the time-mean wind, and the interaction between low-frequency and high-frequency eddies. The term (a) is the baroclinic energy conversion; the term (b) is the ageostrophic geopotential flux convergence; the term (d) is the horizontal advection of EKE by the time-mean wind; the term (e) is the barotropic conversion.

Fig. 9.

Figure 9 displays horizontal distribution of the terms in Eq. (4) for M30. In Fig. 9, a positive (negative) sign means that high-frequency eddies gain (lose) their kinetic energy. The baroclinic energy conversion (Fig. 9a) is dominant and closely follows the distribution of the near-surface baroclinicity (Fig. 7a), designating the importance of the near-surface baroclinicity for the enhancement of the storm activity. The ageostrophic motion in baroclinic eddies radiates the EKE toward the equator as indicated by the ageostrophic geopotential flux in Fig. 9b. Baroclinic eddies tend to lose their EKE strongly by sea surface friction between 30°N and 35°N (Fig. 9c). Both the horizontal advection of EKE and the

barotropic energy conversion are much smaller and insignificant for the storm track localization (Figs. 9d and 9e). The insignificant zonal asymmetry of the barotropic energy conversion also suggests the negligible effect of the stationary eddies for the localization of the storm track at least in our model.

Toward the east end of the storm track (east of 180°), the baroclinic conversion becomes small. The ageostrophic EKE radiation and surface friction contribute about equally to diminishing transient eddy, while the barotropic conversion plays a minor role for the storm track termination in our model.

5. Feedback between transient and stationary eddies

Large zonal variations in the mid-latitude storm activity in M30 can conceivably affect stationary waves by transient-eddy heat and vorticity fluxes, or by modulating condensational heating due to precipitation which is highly correlated with the SST anomaly itself. In this section, we analyze heat and vorticity budgets to determine key processes for the formation of stationary waves in our model.

a. Heat budget

The zonally asymmetric component of the time-mean thermodynamic equation is written as,

$$\underbrace{\left(\overline{u}\frac{\partial\overline{\theta}}{\partial x}\right)^*}_{\text{(a)}} + \underbrace{\left(\overline{v}\frac{\partial\overline{\theta}}{\partial y}\right)^*}_{\text{(b)}} + \underbrace{\left(\overline{\omega}\frac{\partial\overline{\theta}}{\partial p}\right)^*}_{\text{(c)}} +$$

$$\underbrace{\left(\nabla \cdot (\overline{\boldsymbol{u}'\theta'}) \right)^*}_{\text{(d)}} = \underbrace{\left(\overline{\mathcal{Q}} \right)^*}_{\text{(e)}}, \tag{5}$$

where the asterisk denotes the departure from zonal mean, θ is potential temperature, and $\mathcal{Q}$ is diabatic heating which is estimated as the residual of Eq. (5). The terms (a)–(c) in Eq. (5) mean zonally asymmetric components of zonal, meridional, and vertical advection of potential temperature; the term (d) is transient-eddy heat flux divergence.

Fig. 10.

Figure 10 displays the longitude-pressure cross section of the terms in Eq. (5) along 40°N for M30. Throughout the troposphere, transient-eddy heat flux convergence is generally much smaller than the other terms[2]. In the lower half of the troposphere, zonally varying diabatic heating, mainly due to large-scale condensation accompanied with synoptic activity (not shown), balances the zonal advection term. In the mid-troposphere around 500 hPa, terms (b) and (c) also have a significant magnitude. Near the tropopause, diabatic heating is small, and the meridional advection term is in balance with the vertical and zonal advection terms.

Since $[\overline{u}]\dfrac{\partial \overline{\theta}^*}{\partial x}$ is proportional to $-\dfrac{[\overline{u}]}{f}\dfrac{\partial \overline{v}^*}{\partial p}$ where the square bracket denotes the zonal mean, the zonal advection term is associated with the zonal variation of meridional wind velocity. We expect the stationary-eddy northerly around 60°E and 40°N, consistent with a stationary-eddy anti-cyclone around 120°E (Fig. 6a). Moreover, the upward (downward) motion in the region of anomalous condensational heating (cooling) north of the warm (cool)

[2]With the transient-eddy heat flux peaking at the storm track axis (40°N; Fig. 5b), its convergence reaches a maximum around 50°N. Even at 50°N, transient-eddy heat flux convergence is only a secondary term in the lower troposphere heat budget (not shown).

SST anomaly is important for the maintenance of lower tropospheric stationary eddies as shown below.

b. Vorticity budget

The zonally asymmetric component of the time-mean vorticity equation is written as,

$$\underbrace{\left(\overline{u}\frac{\partial\overline{\zeta}}{\partial x}\right)^*}_{(a)} + \underbrace{\left(\tilde{\beta}\,\overline{v}\right)^*}_{(b)} + \underbrace{\left(f\overline{D}\right)^*}_{(c)} + \underbrace{\left(\nabla\cdot(\overline{\boldsymbol{u}'\zeta'})\right)^*}_{(d)} = \underbrace{\left(\overline{\mathcal{F}}\right)^*}_{(e)}, \tag{6}$$

where $D = \dfrac{\partial u}{\partial x} + \dfrac{\partial v}{\partial y}$, $\zeta = \dfrac{\partial v}{\partial x} - \dfrac{\partial u}{\partial y}$, $\tilde{\beta} = \dfrac{\partial}{\partial y}(f + \overline{\zeta})$, and $\mathcal{F}$ is regarded as the terrestrial friction of vorticity, which is obtained as the residual of Eq. (6). The terms (a) and (b) in Eq. (6) indicate the zonal and meridional advection of the time-mean absolute vorticity, respectively; the term (c) denotes the stretching of the time-mean vortex tube; the term (d) is transient-eddy vorticity flux divergence.

Fig. 11.

Figure 11 displays the longitude-pressure cross section of the terms of Eq. (6) along 40°N for M30. Indeed, vortex stretching is most important for the generation of stationary eddies in both the upper and lower troposphere. Throughout the troposphere, the transient-eddy flux convergence [the term (d)] is quite noisy and its WN-1 component is much smaller than the other terms. The vorticity flux divergence associated with the transient eddies is therefore insignificant for generating stationary eddies in our model[3]. In the upper troposphere, the vortex stretching term roughly balances with zonal advection term. With

[3]The convergence transient-eddy vorticity flux is quite large on the either side of the storm track axis. Especially at 50°N–60°N, it is actually comparable to the other terms in the upper troposphere. In the

strong vortex squeezing (stretching) taking place around 90°E (90°W), a stationary high (low) forms downstream, consistent with the heat budget. In the mid-troposphere, the vortex stretching term becomes insignificant and a balance between zonal and meridional advection term is dominant.

Fig. 12.

In the lower troposphere, vortex stretching is mainly balanced with the terrestrial friction. At 40°N, anomalous stretching (squeezing) around 90°E (90°W) leads to a surface low (high) in Fig. 5. Figure 12a shows the horizontal distribution of diabatic heating at 500 hPa, which appears to be correlated with the vortex stretching term at 850 hPa in the planetary-scale distribution (Fig. 12b). For example, along 40°N, the diabatic heating (cooling) in 0°–120°E (180°–60°W) is associated with vortex stretching (squeezing). Furthermore, the heating and stretching anomalies both show a tendency to extend northeastward from 40°N. With negligible SST anomalies, anomalous diabatic heating is caused by enhanced precipitation in high latitudes due to the convergence of moisture transport by transient eddies (Fig. 8). The stretching field is further well correlated with anomalous geopotential height field in the lower troposphere (Fig. 5a), with a low pressure over the positive precipitation anomaly. This result is quite different from Hoskins and Karoly (1981) and Palmer and Sun (1985), both of who suggested a balance of the vortex stretching term with the beta term near the surface.

c. Positive feedback

The above analysis indicates a positive feedback mechanism between transient and sta-

---

lower troposphere, it is secondary in the vorticity balance. See Appendix B for a qualitative estimate of vorticity flux using the E-vector diagnosis.

tionary eddies in the M30 experiment. SST-induced zonal variations in the synoptic eddy activity generate stationary eddies through condensational heating in the storm track, which in turn reinforces the zonal variations in vertical shear that controls the storm track. This feedback process is somewhat consistent with Hoskins and Valdes (1990) suggesting the importance of diabatic heating for maintaining the low level baroclinicity, which in turn localizes the storm track.

Both high SST gradient and high SST (through its control of surface humidity) are necessary for the above feedback mechanism to operate. In M30 along the axis of the storm track (40°N), the zonal maxima in SST gradient and SST coincide, leading to strong zonal variations in storm activity, precipitation and time-mean flow. In M50, by contrast, the zonal maximum in SST gradient coincides with the zonal minimum in SST along 40°N, resulting in a zonally uniform storm track and weak stationary eddies. We plan to use a simpler mechanistic model to establish the causal relationship between the deep heating and the storm track, and to examine the relevance of these feedback processes outlined here in the real atmosphere.

6. Application to the real atmosphere

a. Southern Hemisphere

With little land and elevation below 1.5 km between 40°S and 65°S, the mid-latitude SH is close to aqua-planet conditions used in our AGCM experiments. In austral winter, the SH westerlies clearly split into subtropical and subpolar jet streams (Fig. 1c). Centered at 27°S,

the subtropical jet core is located in the eastern Indian and western Pacific Oceans sector, probably because of an enhanced Hadley circulation south of intense convection associated with the Asian-western Pacific summer monsoon. The storm activity is strongest in the east Atlantic and Indian Ocean sector, poleward and *upstream* of the subtropical jet core (Fig. 1b). The relative location between SH storm track and subtropical jet core is puzzling in light of NH climate but consistent with results from our aqua-planet experiments. As in our experiments, the SST distribution of the mid-latitude oceans in the SH is dominated by a WN-1 structure, with maximum meridional SST gradient in the Atlantic and Indian Oceans sector (Fig. 1a). Indeed, the SH storm track develops over and downstream of this zone of strong SST gradient, much as in our aqua-planet AGCM. NS show that the SH storm track correlates better with baroclinicity near the sea surface than that above the PBL, which is related to SST gradient and the subtropical jet, respectively. This good correlation between storm activity and near-surface baroclinicity holds on both the seasonal and interannual timescales.

While neglected in our experiments completely, tropical SST is clearly a factor for SH climate as attested by the existence of the subtropical jet cores there. The Antarctica, the ice-covered uplift, is an apparent strong forcing as well. Unlike the M30 experiment, the SH has these surface conditions, which are quite effective to stationary eddies and localized storm tracks. The stationary waves in austral winter (Figs. 1d and 1e) are almost equivalent barotropic, quite different from M30's stationary waves with baroclinic structure (Figs. 4a and 5a). Thus the proposed feedback mechanism in Section 5c may not be directly applicable to the SH storm track formation, so that the similarity between the SH and M30

is limited to the relationship between mid-latitude SST and storm tracks. We plan to study more carefully the effects of tropical and extratropical SST and orographic forcing on SH stationary and transient eddies, in order to investigate what makes the difference between the SH and the aqua-planet experiment.

b. Northern Hemisphere

NH wintertime storm tracks, by contrast, are located downstream of the subtropical jet core (Blackmon et al. 1977), opposite to their relation in the SH and in the M30 run of our aqua-planet AGCM. This suggests that large-scale orography is probably the first order factor for NH storm track. Nevertheless, this SST effect is detectable in certain cases. Performing ensemble simulations with a high-resolution regional model, Xie et al. (2002) show that over the western North Pacific, a winter storm grows significantly stronger along the Kuroshio front than in the ensemble with reduced SST gradient, a result consistent with the concept of SST modulation of storm activity we have demonstrated here in a global AGCM.

c. Air-sea interaction

A key issue to current research on extratropical climate variability is whether and how the atmosphere reacts to SST changes in the extratropics. Our results show that there is a significant response in both stationary and transient eddies if the SST effects on precipitation and baroclinicity reinforce each other (as in the M30 run). Consistent with previous studies, this response is sensitive to the relative location of the SST anomalies and existing storm track.

Fig. 13.

Here we broaden our discussion by inferring the atmospheric feedback on imposed SST anomalies. Figure 13 shows anomalous wind stress and its curl superimposed on the zonal variations of SST for M30. The westerly winds intensify (weaken) over the warm (cold) patch, suggesting a negative feedback through surface sensible and latent heat flux. This is distinct from the negative correlation between wind speed and SST forcing that is often observed over the mid-latitude oceans and generally considered to be indicative of one-way atmospheric forcing. The wind-curl feedback on the ocean is less straightforward and unclear at this time since it involves non-local ocean adjustment such as the Rossby wave. We also note that the surface wind response is not limited to the regions with significant SST forcing found elsewhere as well. Such non-local wind response would cause the initial SST forcing pattern to deform in a fully coupled model.

7. Conclusions

Fig. 14.

Aqua-planet AGCM experiments have been conducted to investigate the atmospheric response to zonal variations in mid-latitude SST. The zonal variations of SST are imposed with a WN-1 structure in the zonal and a single-signed monopole structure in the meridional direction. We found that the model response is sensitive to the latitude of the SST forcing relative to the axis of the storm track. When the SST forcing is centered south of the storm track axis (M30), a strong response emerges in both the time-mean field and storm activity, with an upper-tropospheric ridge and enhanced storm activity located northeast of the positive SST forcing center. The resultant storm track is strongly localized in the zonal direction. When the same SST anomaly pattern is shifted to the north of the storm

track axis (M50), by contrast, both the time-mean and the transient eddy response are substantially reduced.

The differences in storm track responses among these experiments are explained by the combined effects of SST on the vertical wind shear and the precipitation, both contributing to low-level baroclinicity. In M30, both effects work in concert to intensify the storm activity north of the positive SST anomaly center. In M50, they compete with each other and exert little net influence on the storm activity. The importance of baroclinicity and moisture process is reported in a recent study of Chang (2001), who shows that condensational heating boosts the growth of baroclinic eddies as the availability of atmospheric moisture increases. These results moreover would imply that a positive feedback between baroclinic eddies and lower-level baroclinicity works through storm-induced precipitation.

The budget analyses also support the positive feedback mechanism. First, the EKE budget analysis confirms that the lower-level baroclinicity enhances the storm activity through baroclinic energy conversion. Next, the heat and vorticity budget analyses indicate that enhanced condensational heating, caused by both increased evaporation over positive SST anomalies and eddy moisture flux, is the most important agent to force stationary eddies in both the upper and lower troposphere. The low-level stationary eddies then in turn strengthen the vertical westerly shear near the surface, giving rise to the zonal variations in baroclinicity and storm activity. The transient-eddy heat and vorticity fluxes play only a secondary role. The above chain of causality is illustrated in Fig. 14a. The proposed feedback is quite different from a previous framework of transient–stationary eddy interaction (Fig. 14b), in which transient eddies play a rather passive role of amplifying pre-existing

stationary waves (Branstator 1995; Peng and Whitaker 1999). This conventional interaction prevails when stationary-wave forcing by orography and/or tropical deep convection dominates as in the NH. In the mid-latitudes, the direct atmospheric response to SST changes is probably trapped in the PBL because of the stable stratification. The transient–stationary eddy feedback mechanism proposed here provides another way to transform this shallow direct response to a deep one over the whole depth of the troposphere.

The feedback hypothesis proposed here explains the strongest storm activity located south of an upper-tropospheric ridge with a weak subtropical jet (Figs. 4a and 4b), a result opposite to the observed winter climatology in the NH where storm activity tends to increase at and downstream of the subtropical jet core (Chang et al. 2002; Solman and Menéndez 2002). This model result is, however, consistent with a recent analysis of SH storm tracks. In austral winter, the SH storm track is located south of Africa, upstream of the subtropical jet core centered at the International Dateline. NS show that both in space and on seasonal and interannual timescales, storm activity is highly correlated with near-surface baroclinicity, but not with the subtropical jet. While orography seems very important for NH storm tracks, without large landmass in the mid- and high latitudes of the SH, the storm track dynamics there seem quite similar to those in our aqua-planet AGCM. It is an interesting area of research to further explore the storm track and stationary eddy dynamics in the SH.

Acknowledgments. We wish to thank K. Yamazaki, M. Kimoto, Y. Tanimoto, M. Watanabe, F. Hasebe, J. Yin, and anonymous reviewers for insightful comments that helped improve

the manuscript. We also wish to thank M. Kimoto for using CCSR/NIES AGCM version 5.5b. This study was supported by Japan Society of Promoting Sciences through Grants-in-Aid for Scientific Research (C) (2) 12640417 and Scientific Research on Priority Areas (B) (2) 11219203, Center for Climate System Research of University of Tokyo, Frontier Research System for Global Change, U.S. National Science Foundation (ATM-0104468), and National Science Foundation of China (40240420564). The figures were produced with the GFD-DENNOU Library.

Appendix A

Statistical significance test

Statistical significance test in section 3 is done with the following procedure. First, we equally divide the 1500-day model output into 10 subsets. The initial 90-day record in each subset is retained while the remainder is discarded. These 90-day subsets, $\{q_n(\lambda, \phi, p, t)\}$ $(n = 1, 2, ..., 10)$, are thus considered to be independent of each other. We then compute the 90-day average and its zonal deviation, $\{\overline{q_n}^*(\lambda, \phi, p)\}$. The student t-test is applied to the null hypothesis of "$\sum_{n=1}^{10} \overline{q_n}^*(\lambda, \phi, p) = 0$." At each gridpoint, when the t-value calculated from the 10 independent subsets is less than 2.262, the null hypothesis is rejected with 95% statistically significant level and the zonally asymmetric component can be regarded as nonzero.

Appendix B

The E-vector diagnosis

The E-vector,

$$\boldsymbol{E} = \left(\frac{\overline{v'^2 - u'^2}}{2},\ -\overline{u'v'},\ \frac{f}{\partial\overline{\theta}/\partial p}\overline{v'\theta'} \right), \tag{7}$$

is used for a qualitative diagnosis for the propagation of transient eddies and their feedback effect onto the time-mean flow. It is approximately proportional to the group velocity of the Rossby wave, and its divergence (convergence) indicates the acceleration (deceleration) of the time-mean zonal wind (Trenberth 1986). Note that transient-eddy vorticity flux divergence [the term (d) in Eq. (6)] approximates to $\frac{\partial}{\partial y}\nabla_{\mathrm{H}} \cdot \boldsymbol{E}$.

Fig. B1.

Figure B1a displays the longitude-pressure cross section of the E-vector together with storm activity along 40°N for M30. Near the surface, the E-vector attains its maximum magnitude and directs upward around 90°E, indicative of low-level baroclinic development (Fig. 9a). The feedback onto the mean flow tends to destroy vertical westerly wind shear in the lower troposphere. In the upper troposphere, eddy activity propagates eastward with a smaller vertical component. Figure B1b shows the E-vector and its divergence on 250 hPa. Transient eddies propagate downstream and equatorward from the center of the storm track. The E-vector diverges (converges) just at (south of) the storm track axis, accelerating (decelerating) the time-mean westerly flow in (south of) the storm track region. However, the westerly acceleration is rather zonally uniform. Furthermore the barotropic energy conversion, simply estimated by $-\overline{u'v'}\frac{\partial\overline{u}}{\partial y}$, is positive (negative) just north (south) of subtropical westerly jet, consistent with the EKE budget analysis (Fig. 9e). The E-vector

diagnosis here shows the general propagation characteristic of synoptic eddies in the NH winter (Hoskins et al. 1983).

The equatorward E-vectors dominate along the storm track axis (40°N), much stronger than the poleward ones in higher latitudes. This implies a much higher probability of occurrence for synoptic eddies propagating toward the equator (the LC2-type lifecycle in Thorncraft et al. 1993) than the LC1-type ones breaking to the north of the storm track. Akahori and Yoden (1997) suggested that whether synoptic eddies prefer the LC1 or LC2 cycle depends upon the relative meridional position between subtropical jet and storm track. In our experiments, the storm track axis is located to the north of subtropical jet, which is a configuration in favor of the LC2 cycle and similar to what is observed over the winter-time North Pacific.

References

Akahori, K., and S. Yoden, 1997: Zonal flow vacillation and bimodality of baroclinic eddy life cycles in a simple global circulation model. *J. Atmos. Sci.*, **54**, 2349–2361.

Arakawa, A., and W. H. Schubert, 1974: Interaction of cumulus cloud ensemble with the large-scale environment. Part I. *J. Atmos. Sci.*, **31**, 674–701.

Blackmon, M. L., 1976: A climatological spectral study of the 500 mb geopotential height of the Northern Hemisphere. *J. Atmos. Sci.*, **33**, 1607–1623.

——, J. M. Wallace, N.-C. Lau, and S. L. Mullen, 1977: An observational study of the Northern Hemisphere wintertime circulation. *J. Atmos. Sci.*, **34**, 1040–1053.

Branstator, G., 1995: Organization of storm track anomalies by recurring low-frequency circulation anomalies. *J. Atmos. Sci.*, **52**, 207–226.

Chang, E. K. M., 2001: GCM and observational diagnoses of the seasonal and interannual variations of the Pacific storm track during the cool season. *J. Atmos. Sci.*, **58**, 1784–1800.

——, S. Lee, and K. L. Swanson, 2002: Storm Track Dynamics. *J. Climate*, **15**, 2163–2183.

Eady, E. A., 1949: Long waves and cyclone waves. *Tellus*, **1**, 33–52.

Gutowski, W. J., L. E. Branscome, and D. A. Stewart, 1992: Life cycles of moist baroclinic eddies. *J. Atmos. Sci.*, **49**, 306–319.

Held, I. M., 1983: Stationary and quasi-stationary eddies in the extratropical troposphere: Theory. *Large-Scale Dynamical Processes in the Atmosphere,* B. J. Hoskins and R. Pearce, Eds., Academic Press, 127–168.

Hoskins, B. J., and D. J. Karoly, 1981: The steady linear response of a spherical atmosphere to thermal and orographic forcing. *J. Atmos. Sci.*, **38**, 1179–1196.

——, and P. J. Valdes, 1990: On the existence of storm-tracks. *J. Atmos. Sci.*, **47**, 1854–1864.

——, I. N. James, and G. H. White, 1983: The shape, propagation, and mean-flow interaction of large-scale weather systems. *J. Atmos. Sci.*, **40**, 1595–1612.

Inatsu, M., H. Mukougawa, and S.-P. Xie, 2002a: Stationary eddy response to surface boundary forcing: Idealized GCM experiments. *J. Atmos. Sci.*, **59**, 1898–1915.

——, ——, and ——, 2002b: Tropical and extratropical SST effects on the midlatitude storm track. *J. Meteor. Soc. Japan*, **80**, 1069–1076.

Kushnir, Y., and I. M. Held, 1996: Equilibrium atmospheric response to North Atlantic SST anomalies. *J. Climate*, **9**, 1208–1220.

——, W. A. Robinson, I. Bladé, N. M. J. Hall, S. Peng, and R. Shutton, 2002: Atmospheric GCM response to extratropical SST anomalies: Synthesis and evaluation. *J. Climate*, **15**, 2233–2256.

Le Treut, H., and Z.-X. Li, 1991: Sensitivity of an atmosphere general circulation model to prescribed SST changes: Feedback effects associated with the simulation of cloud optical properties. *Clim. Dyn.*, **5**, 175–187.

Lindzen, R. S., and B. Farrell, 1980: A simple approximate result for the maximum growth rate of baroclinic instabilities. *J. Atmos. Sci.*, **37**, 1648–1654.

Louis, J., 1979: A parametric model of vertical eddy fluxes in the atmosphere. *Bound. Layer Meteor.*, **17**, 187–202.

Manabe, S., and T. B. Terpstra, 1974: The effects of mountains on the general circulation of the atmosphere as identified by numerical experiments. *J. Atmos. Sci.*, **31**, 3–39.

McFarlane, N. A., 1987: The effect of orographically excited wave drag on the general circulation of the lower stratosphere and troposphere. *J. Atmos. Sci.*, **44**, 1775–1800.

Mellor, G. L., and T. Yamada, 1982: A hierarchy of turbulence closure model for geophysical fluid problems. *Rev. Geophys. Atmos. Phys.*, **20**, 851–875.

Nakajima, T., and M. Tanaka, 1988: Matrix formulation for the transfer of solar radiation in a plane-parallel scattering atmosphere. *J. Quant. Spectrosc. Radiat. Transfer*, **35**, 12–21.

Nakamura, H., and A. Shimpo, 2002: Seasonal variations in the Southern Hemisphere storm tracks and jet stream as revealed in a reanalysis data set. *J. Climate*, submitted.

Numaguti, A., 1999: Origin and recycling process of precipitating water over the Eurasian continent: Experiment using an atmospheric general circulation model. *J. Geophys. Res.*, **104**, 1957–1972.

——, M. Takahashi, T. Nakajima, and A. Sumi, 1997: Description of CCSR/NIES atmospheric general circulation model. CGER Supercomputer Monograph Report, **3**, 1–48, National Institute for Environmental Studies, Tsukuba, Japan.

Palmer, T. N., and Z. Sun, 1985: A modelling and observational study of the relation-

ship between sea surface temperature in the north-west Atlantic and the atmospheric general circulation. *Quart. J. Roy. Meteor. Soc.*, **111**, 947–975.

Peng, S., and J. S. Whitaker, 1999: Mechanism determining the atmospheric response to midlatitude SST anomalies. *J. Climate*, **12**, 1393–1408.

——, W. A. Robinson, and M. P. Hoerling, 1997: The modeled atmospheric response to midlatitude SST anomalies and its dependence on background circulation states. *J. Climate*, **10**, 971–987.

Robinson, W. A., 2000: Review of WETS – The Workshop on extra-tropical SST anomalies. *Bull. Amer. Meteor. Soc.*, **81**, 567–577.

Simmons, A. J., 1982: The forcing of stationary wave motion by tropical diabatic heating. *Quart. J. Roy. Meteor. Soc.*, **108**, 503–534.

Solman, S. A., and C. G. Menéndez, 2002: ENSO-related variability of the Southern Hemisphere winter storm track over the eastern Pacific-Atlantic sector. *J. Atmos. Sci.*, **59**, 2128–2140.

Thorncraft, C. D., B. J. Hoskins, and M. E. McIntyre, 1993: Two paradigms of baroclinic-waves life-cycle behaviour. *Quart. J. Roy. Meteor. Soc.*, **119**, 17–55.

Trenberth, K. E., 1986: An assessment of the impact of transient eddies on the zonal flow during a blocking episode using localized Eliassen-Palm flux diagnosis. *J. Atmos. Sci.*, **43**, 2070–2087.

Valdes, P. J., and B. J. Hoskins, 1989: Linear stationary wave simulation of the time-mean climatological flow. *J. Atmos. Sci.*, **46**, 2509–2527.

Xie, S.-P., J. Hafner, Y. Tanimoto, W. T. Liu, H. Tokinaga, and H. Xu, 2002: Bathymetric effect on the winter sea surface temperature and climate of the Yellow and East China Seas. *Geophys. Res. Lett.*, **29, 2228**, doi:10.1029/2002GL015884.

Captions of Figures

FIG. 1. (a) Climatological-mean SST for July based upon the GISST data set from 1950 to 1999. Contour intervals are 2 K with 8–16 K shaded. (b) Climatological-mean storm track on 250 hPa for July based upon ECMWF Reanalysis twice-daily data from 1979 to 1993. Contour intervals are 10 m and shading is > 80 m. (c) Same as b, but for zonal wind. Contour intervals are 5 m s^{-1} and shading is > 40 m s^{-1}. (d) Same as b, but for 250 hPa geopotential height with contour interval 20 m and light (heavy) shading > 80 m (< -80 m). (e) Same as d, but for 850 hPa with contour interval 10 m and light (heavy) shading > 40 m (< -40 m).

FIG. 2. SST (contour) and its deviation from the zonal mean (shading) for (a) the M30, (b) the M40, and (c) the M50 experiments. Labels for contours are measured by degree Celsius and contour interval is 1 K. The shadings are as the gray scale on the bottom for reference.

FIG. 3. The latitude-height cross section of zonal-mean zonal wind for M30 (a), M40 (b), and M50 (c; contour) and difference from that for the control run (shading). Contour intervals are 5 m s^{-1} with negative contours dashed. The light and heavy shadings denote > 2 m s^{-1} and < -2 m s^{-1}, respectively.

FIG. 4. Stationary-eddy geopotential height (contour) and $> 95\%$ significant levels in the t-statistics in geopotential height (shading) for (a) M30, (c) M40, and (e) M50. See Appendix A for the way to calculate statistical significance. Contour interval is 10 m with negative contours dashed. Synoptic-scale eddy activity on 250 hPa (contour) and its zonal deviation (shading) for (b) M30, (d) M40, and (f) M50. Synoptic-scale eddy activity is

defined as root-mean-square variance of 2.5–6-day bandpass filtered geopotential height. Contour interval is 5 m. The light and heavy shadings denote > 5 m and < -5 m, respectively.

FIG. 5. Same as Figs. 4a (a), 4c (c), and 4e (e), respectively, but for 850 hPa. Synoptic-scale eddy heat flux for fluctuations with < 10-day period (contour) and its zonal deviation (shading) for (b) M30, (d) M40, and (f) M50. Contour interval is 1 K m s^{-1}. The light and heavy shadings denote > 2 K m s^{-1} and < -2 K m s^{-1}, respectively.

FIG. 6. Same as Fig. 4, but for the longitude-height cross sections at 40°N.

FIG. 7. Vertical derivative of time-mean zonal wind anomaly at 900 hPa (a) and that inferred from the prescribed SST [(b); see the text for the way of calculation] for M30. Contour intervals are 0.2 m s^{-1} $(100\ \text{hPa})^{-1}$ with negative contours dashed. (c) and (d): Same as (a) and (b), but for M40. (e) and (f): Same as (a) and (b), but for M50.

FIG. 8. (a) Sensible heat flux, (b) evaporation, (c) vertically integrated moisture flux divergence ($\|\nabla_{\mathrm{H}} \cdot \overline{\boldsymbol{v}}\,\overline{q}\| + \|\nabla_{\mathrm{H}} \cdot \overline{\boldsymbol{v}'q'}\|$ where $\|\bullet\|$ denotes vertical integration from 900 hPa to 125 hPa), and (d) precipitation for M30. Contour intervals are 5 W m^{-2} with contours > 50 W m^{-2} and < 0 W m^{-2} omitted for (a); 10 W m^{-2} for (b); 2×10^{-5} kg kg^{-1} Pa s^{-1} with negative contours dashed and zero contour omitted for (c); 20 W m^{-2} for (d).

FIG. 9. Vertically integrated high-frequency EKE equation budget for M30: (a) the baroclinic energy conversion, (b) the EKE radiation by the ageostrophic geopotential flux, (c) the mechanical damping of EKE, (d) the horizontal advection of EKE, and (e) the barotropic energy conversion. The vertical integration is executed from 900 hPa to 125 hPa.

These correspond to the terms in Eq. (4), respectively. A positive (negative) value means that high-frequency eddies gain (lose) their kinetic energy. Contour interval is 1 W m^{-2}. The light and heavy shadings denote > 2 W m^{-2} and < -2 W m^{-2}, respectively. Arrows in (b) denote vertically averaged ageostrophic geopotential flux. The reference arrows in the bottom left corner of (b) are 10 m^2 s^{-1} and 10 m^2 s^{-1}.

FIG. 10. Longitudinal-height cross section for zonal deviation of (a) zonal, (b) meridional, and (c) vertical potential temperature advection, (d) transient-eddy heat flux divergence, and (e) time-mean diabatic heating in the time-mean thermodynamical equation at 40°N for M30. These correspond to the terms in Eq. (5), respectively. Contour interval is 0.1 K day^{-1}; negative contours are dashed; the zero contour is removed. The light and heavy shadings denote > 0.6 K day^{-1} and < -0.6 K day^{-1}, respectively.

FIG. 11. Longitude-height cross section for zonal deviation of (a) zonal and (b) meridional advection of time-mean absolute vorticity, (c) vortex-tube stretching term, (d) transient-eddy vorticity flux divergence, and (e) residual averaged over 37–43°N for M30. These correspond to the terms in Eq. (6), respectively. Contour interval is 1×10^{-10} s^{-2}; negative contours are dashed; the zero contour is removed. The light and heavy shadings denote $> 2 \times 10^{-10}$ s^{-1} and $< -2 \times 10^{-10}$ s^{-1}, respectively.

FIG. 12. (a) Same as Fig. 10e, but for horizontal distribution at 500 hPa. (b) Same as Fig. 11c, but for horizontal distribution at 850 hPa.

FIG. 13. Zonally asymmetric wind stress curl (contour), wind stress vector (vector), and SST anomaly (shade). Contour interval is 0.1 N m^{-2} $(100\ day)^{-1}$ with negative contours dashed and zero contour omitted. The reference vectors at the left bottom corner are

0.05 N m^{-2} and 0.05 N m^{-2}. The shade is the same as Fig. 2.

FIG. 14. Illustration for transient eddy–mean flow feedback proposed (a) here and (b) in the previous studies.

FIG. B1. (a) Longitude-height cross section of the E-vector (vector) together with storm track activity (contour) at 40°N for M30. The horizontal and vertical reference arrows in the bottom left corner are 50 m^2 s^{-2} and 5 m^2 s^{-2}. Contour interval is 5 m. (b) Horizontal distribution of the E-vector (vector) and its divergence (contour) at 250 hPa for M30. The horizontal and vertical reference arrows in the bottom left corner are 40 m^2 s^{-2} and 40 m^2 s^{-2}. Contour interval is 1 m s^{-1} day^{-1} with negative contours dashed.

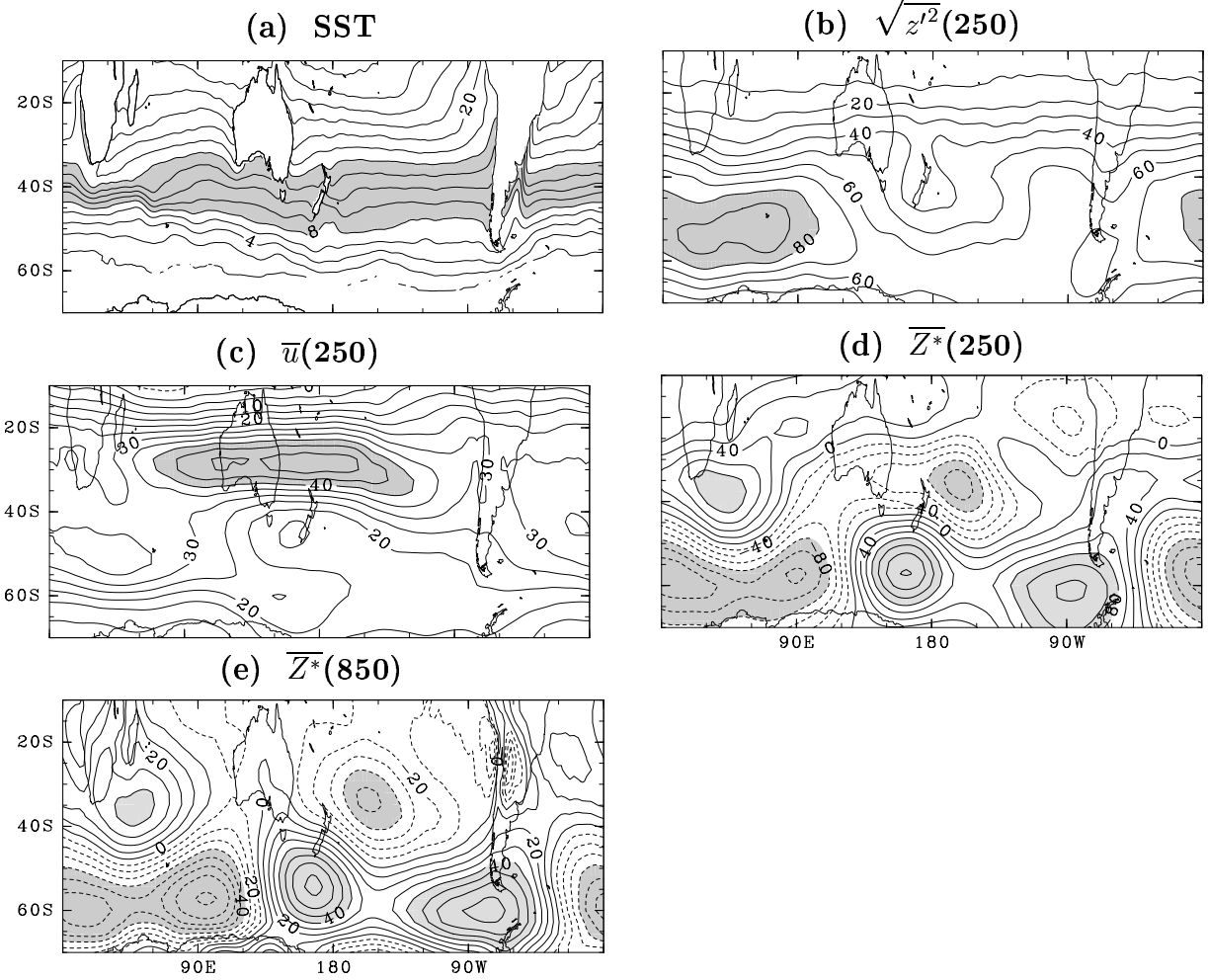
SH July
(a) SST
(b) $\sqrt{\overline{z'^2}}$(250)
(c) $\overline{u}$(250)
(d) $\overline{Z^*}$(250)
(e) $\overline{Z^*}$(850)
20S
40S
60S
90E
180
90W

Fig. 1.

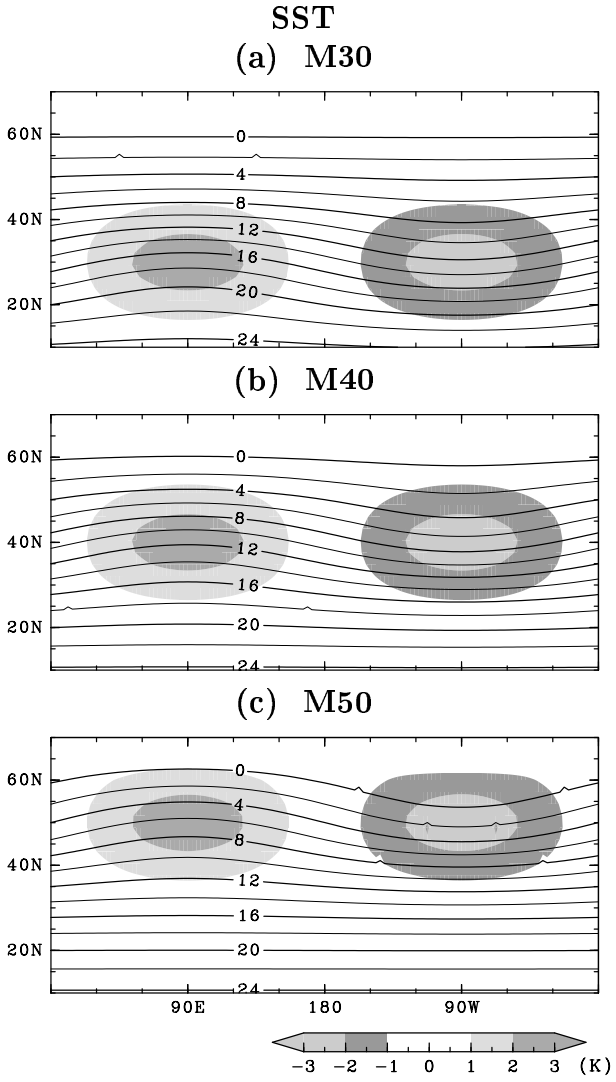
SST
(a) M30
60N
40N
20N
0
4
8
12
16
20
24
(b) M40
60N
40N
20N
0
4
8
12
16
20
24
(c) M50
60N
40N
20N
0
4
8
12
16
20
24
90E
180
90W
−3 −2 −1 0 1 2 3 (K)

Fig. 2.

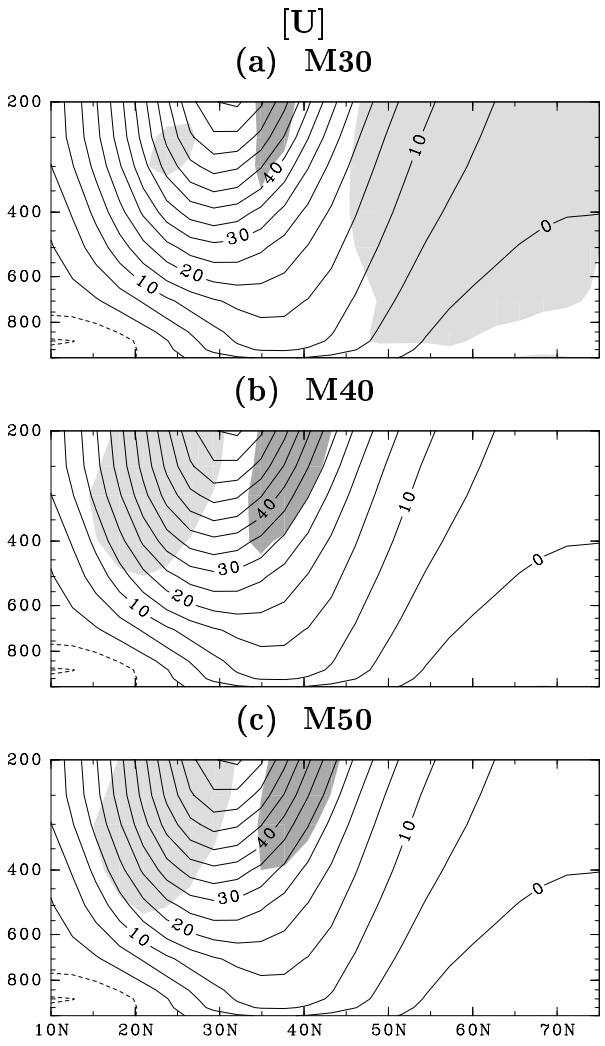
[U]
(a) M30
200
400
600
800
40
30
20
10
10
0
(b) M40
200
400
600
800
40
30
20
10
10
0
(c) M50
200
400
600
800
40
30
20
10
10
0
10N
20N
30N
40N
50N
60N
70N

Fig. 3.

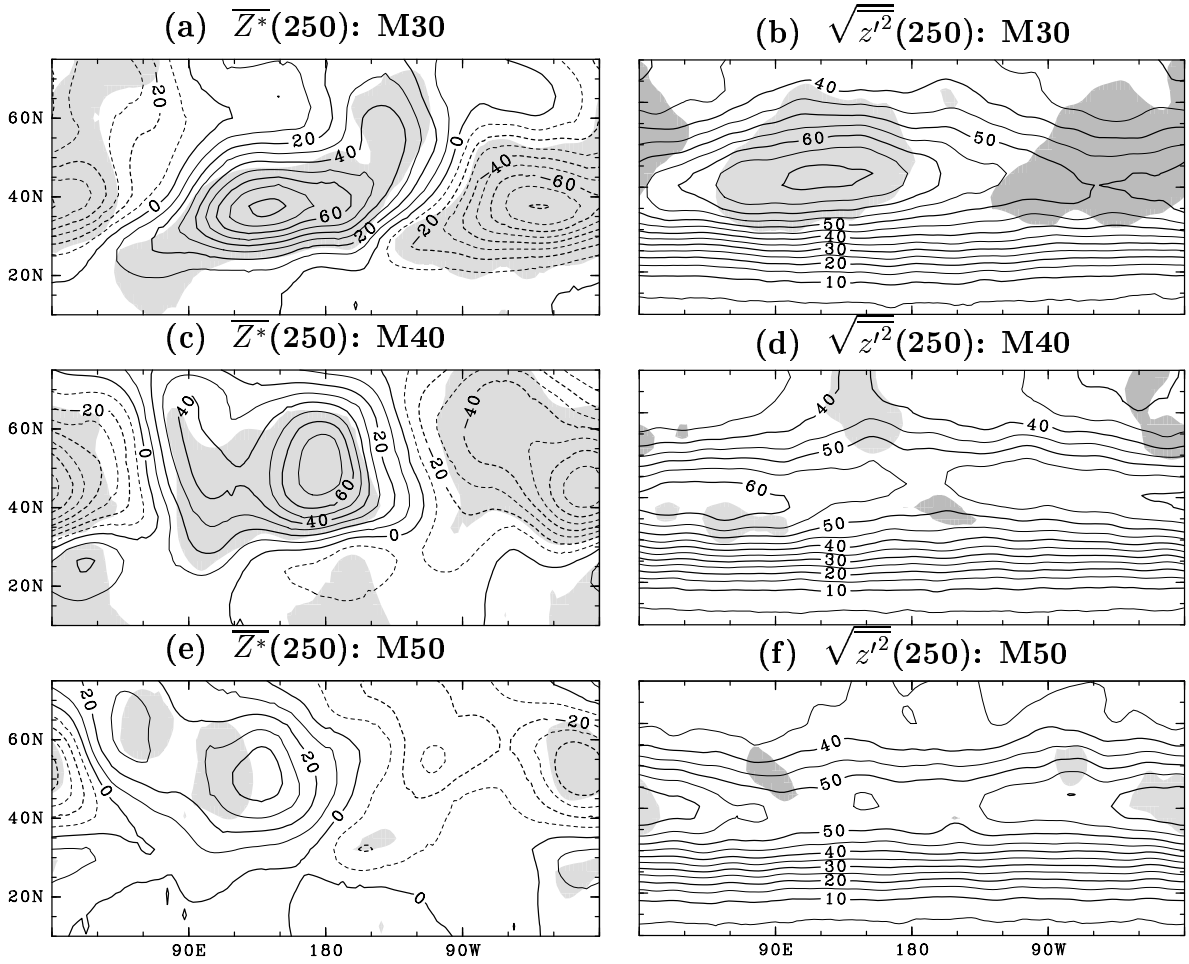
(a) $\overline{Z^*}$(250): M30
(b) $\sqrt{\overline{z'^2}}$(250): M30
(c) $\overline{Z^*}$(250): M40
(d) $\sqrt{\overline{z'^2}}$(250): M40
(e) $\overline{Z^*}$(250): M50
(f) $\sqrt{\overline{z'^2}}$(250): M50
60N
40N
20N
90E
180
90W

Fig. 4.

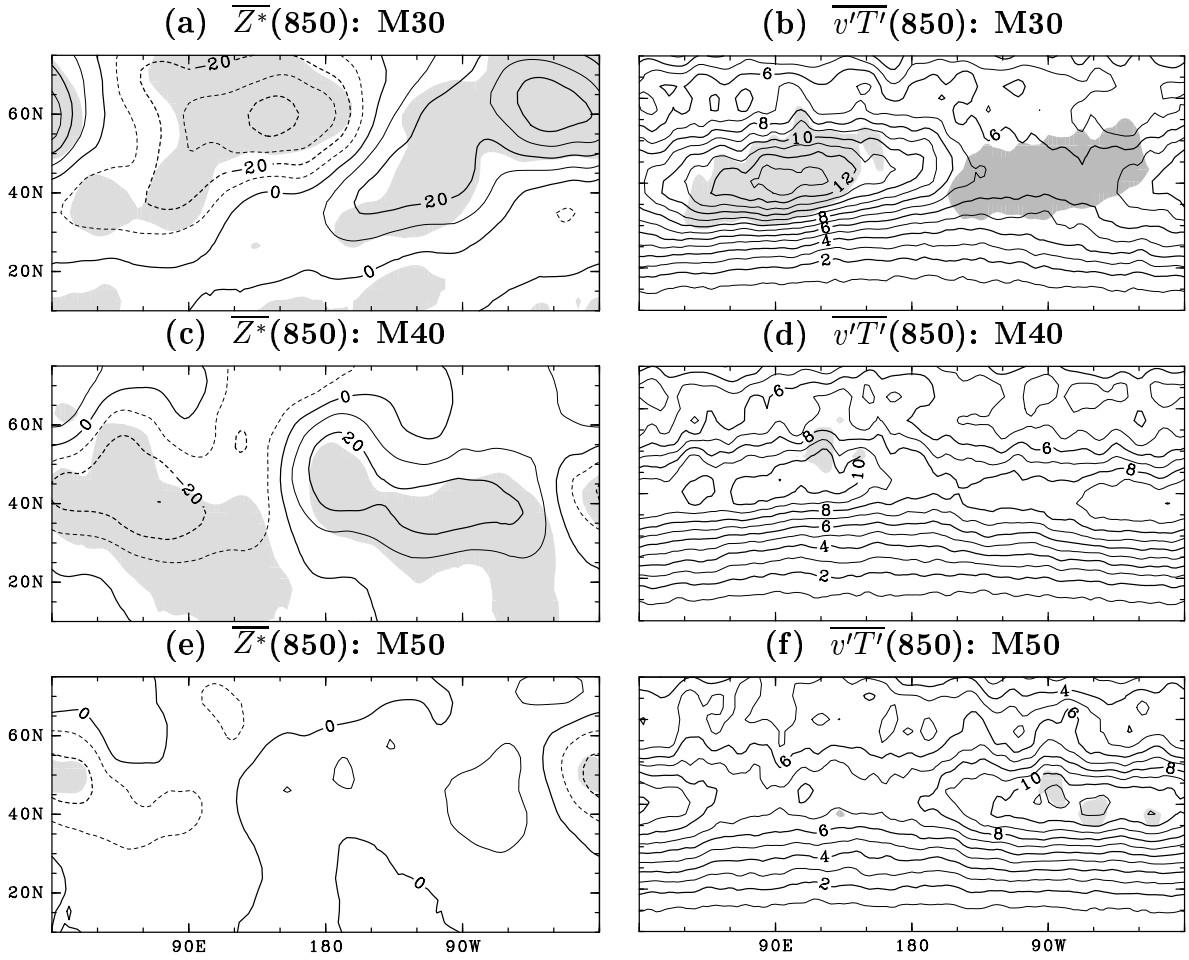
(a) $\overline{Z^*}$(850): M30
(b) $\overline{v'T'}$(850): M30
(c) $\overline{Z^*}$(850): M40
(d) $\overline{v'T'}$(850): M40
(e) $\overline{Z^*}$(850): M50
(f) $\overline{v'T'}$(850): M50
60N
40N
20N
90E
180
90W

Fig. 5.

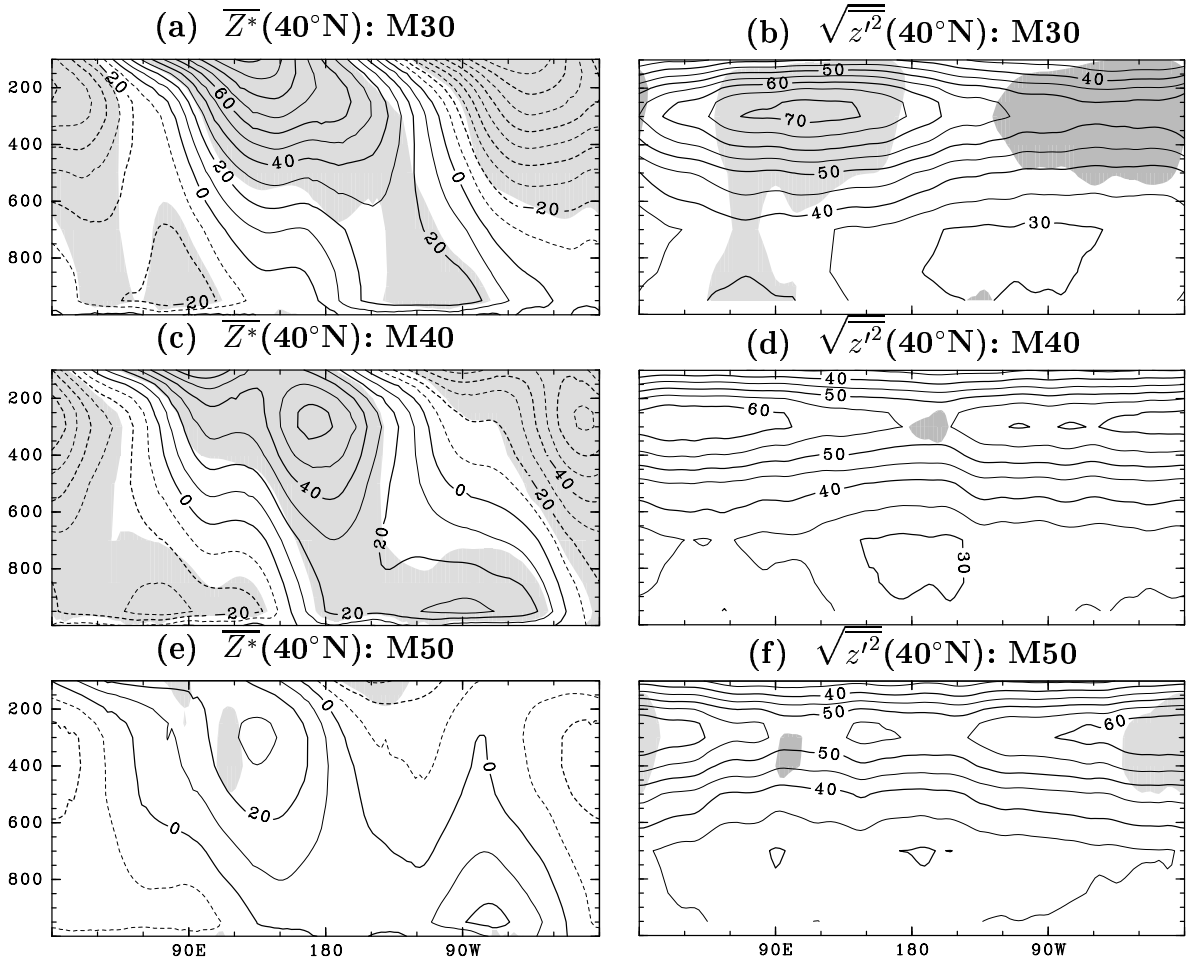
(a) $\overline{Z^*}$(40°N): M30
(b) $\sqrt{\overline{z'^2}}$(40°N): M30
(c) $\overline{Z^*}$(40°N): M40
(d) $\sqrt{\overline{z'^2}}$(40°N): M40
(e) $\overline{Z^*}$(40°N): M50
(f) $\sqrt{\overline{z'^2}}$(40°N): M50
200
400
600
800
90E
180
90W

Fig. 6.

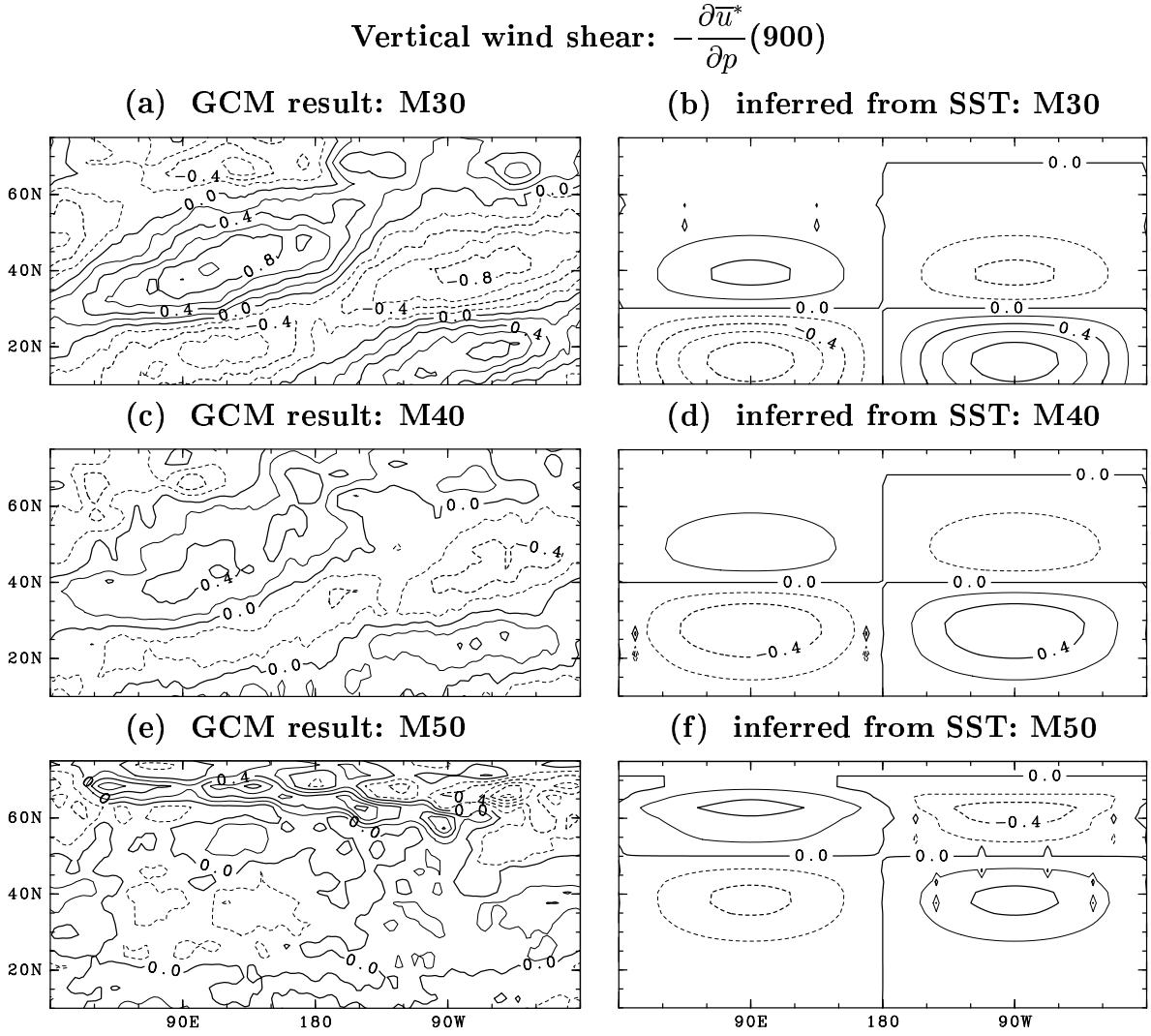
Vertical wind shear: $-\frac{\partial \overline{u}^*}{\partial p}(900)$
(a) GCM result: M30
(b) inferred from SST: M30
(c) GCM result: M40
(d) inferred from SST: M40
(e) GCM result: M50
(f) inferred from SST: M50
60N
40N
20N
90E
180
90W

Fig. 7.

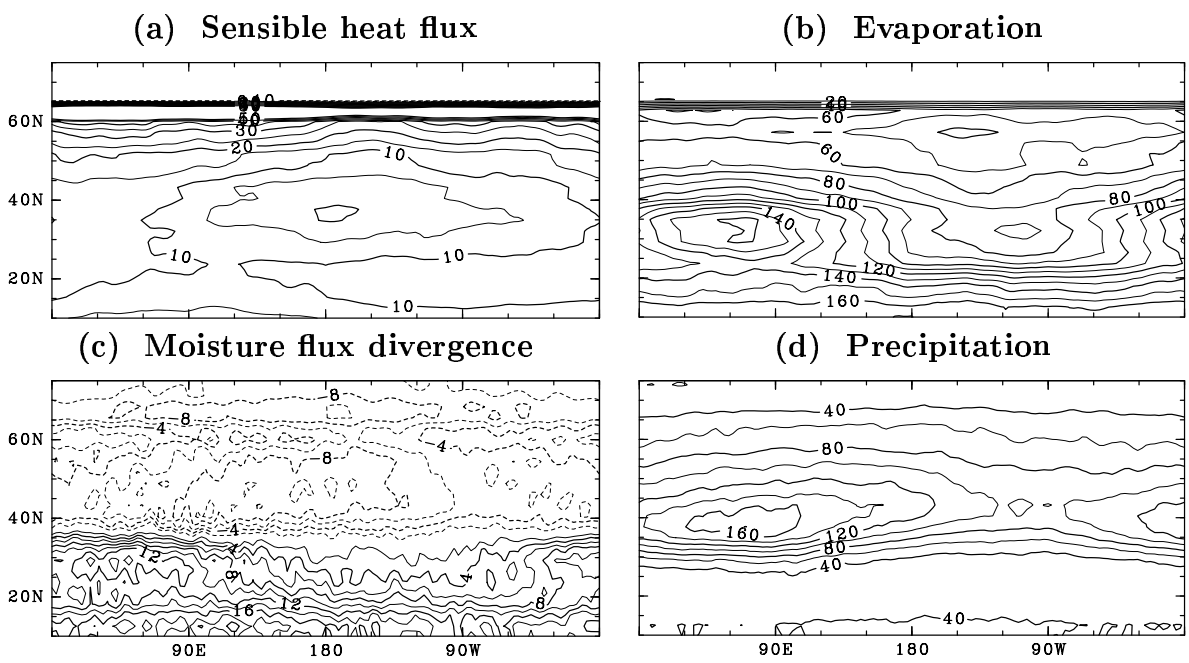
M30
(a) Sensible heat flux
(b) Evaporation
(c) Moisture flux divergence
(d) Precipitation
60N
40N
20N
90E
180
90W

Fig. 8.

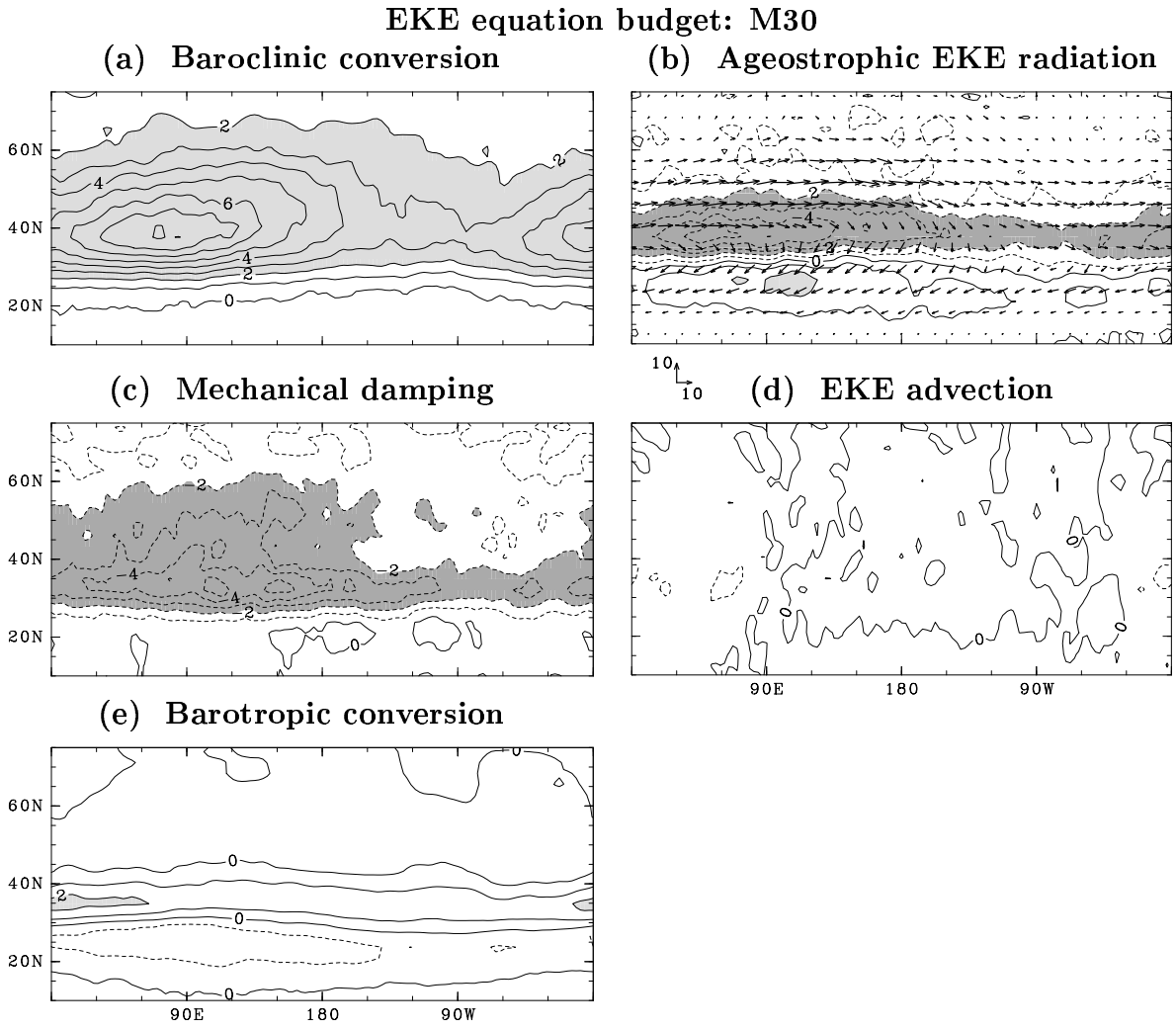
EKE equation budget: M30
(a) Baroclinic conversion
(b) Ageostrophic EKE radiation
(c) Mechanical damping
(d) EKE advection
(e) Barotropic conversion
60N
40N
20N
90E
180
90W
10
10

Fig. 9.

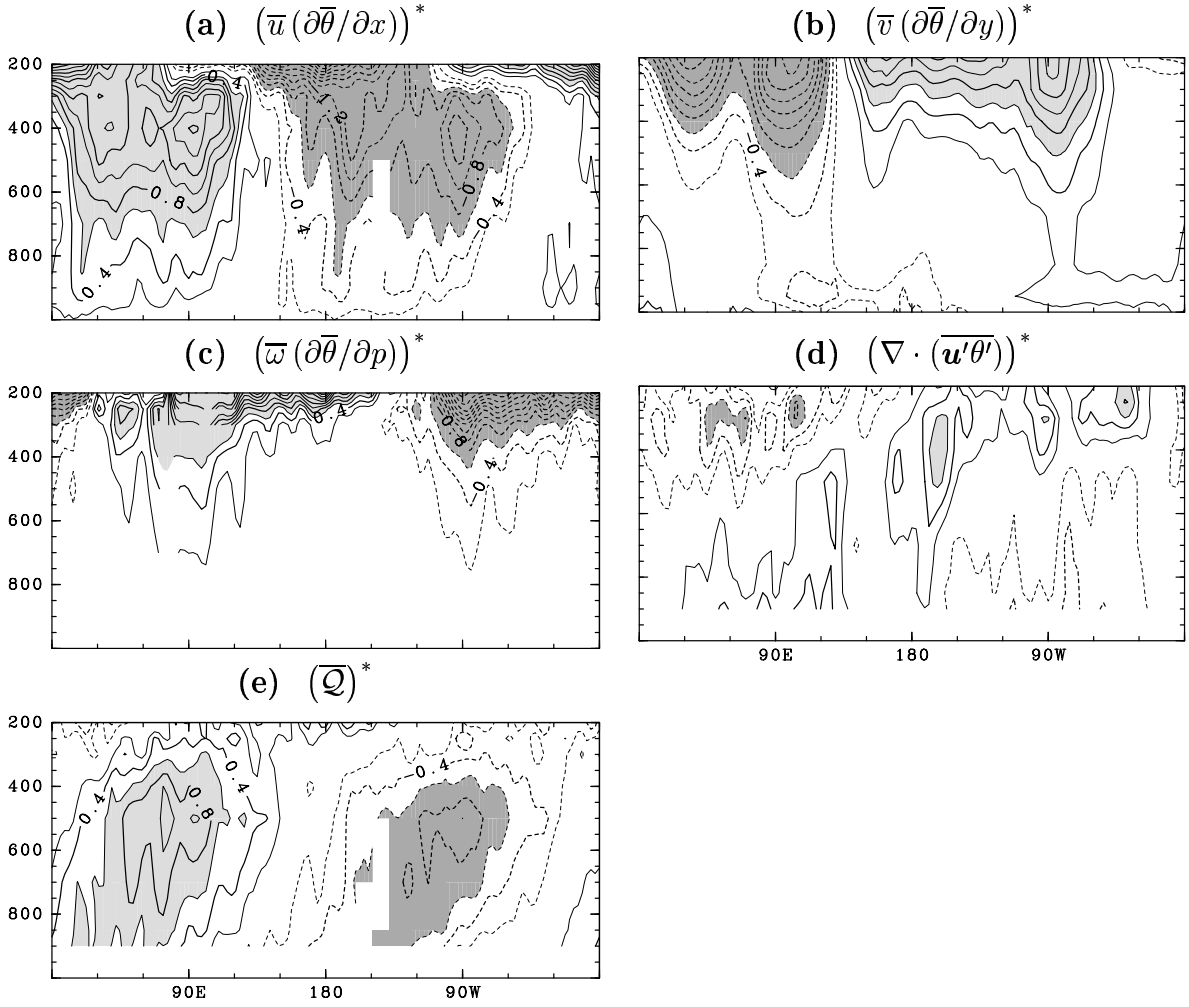
Thermodynamic equation budget at 40°N: M30
(a) $\left(\overline{u}\,(\partial\overline{\theta}/\partial x)\right)^*$
(b) $\left(\overline{v}\,(\partial\overline{\theta}/\partial y)\right)^*$
(c) $\left(\overline{\omega}\,(\partial\overline{\theta}/\partial p)\right)^*$
(d) $\left(\nabla\cdot(\overline{\boldsymbol{u}'\theta'})\right)^*$
(e) $\left(\overline{\mathcal{Q}}\right)^*$
200
400
600
800
90E
180
90W

Fig. 10.

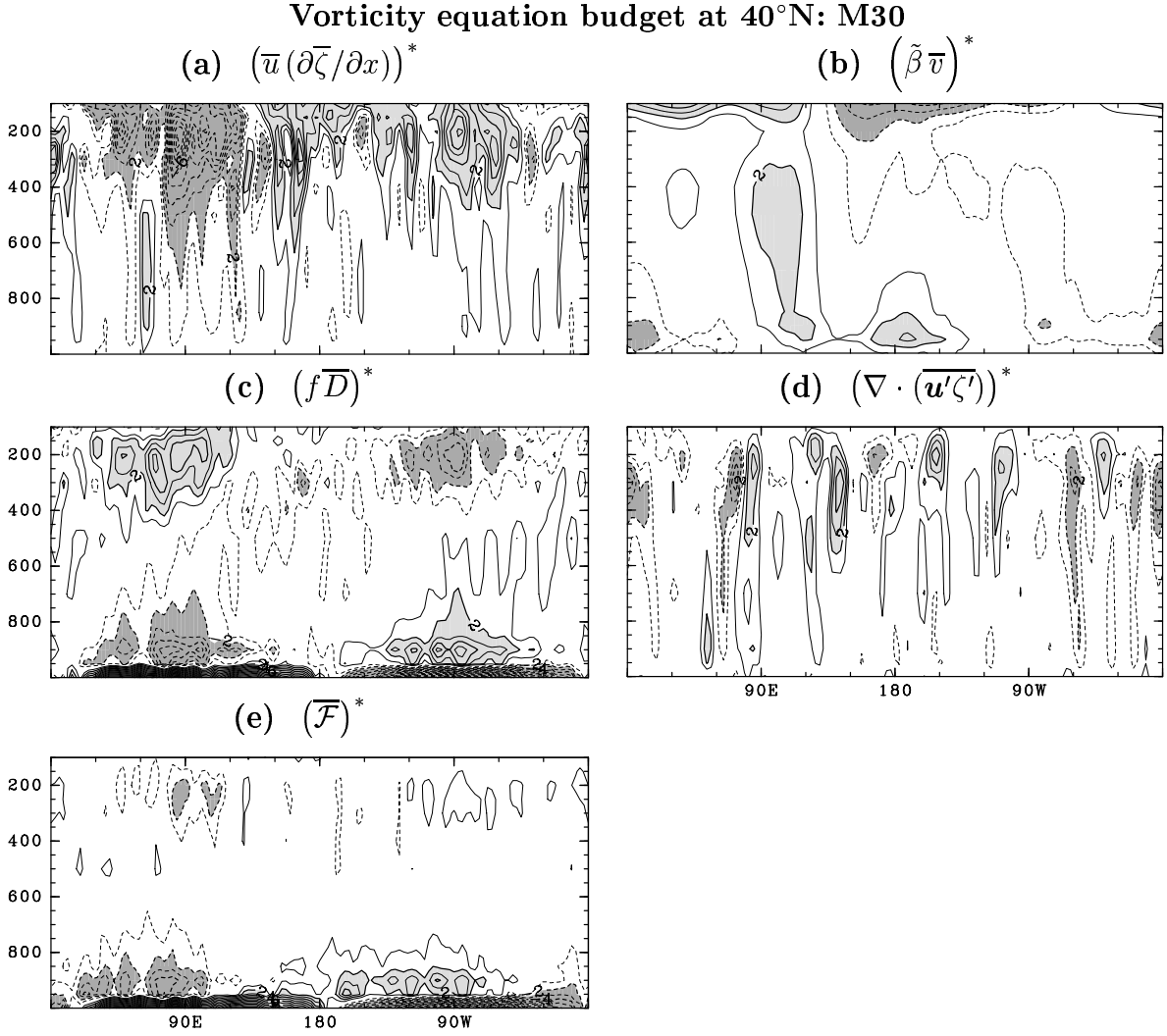
Vorticity equation budget at 40°N: M30
(a) $\left(\overline{u}\,(\partial\overline{\zeta}/\partial x)\right)^*$
(b) $\left(\tilde{\beta}\,\overline{v}\right)^*$
(c) $\left(f\overline{D}\right)^*$
(d) $\left(\nabla\cdot(\overline{\boldsymbol{u}'\zeta'})\right)^*$
(e) $\left(\overline{\mathcal{F}}\right)^*$
200
400
600
800
90E
180
90W

Fig. 11.

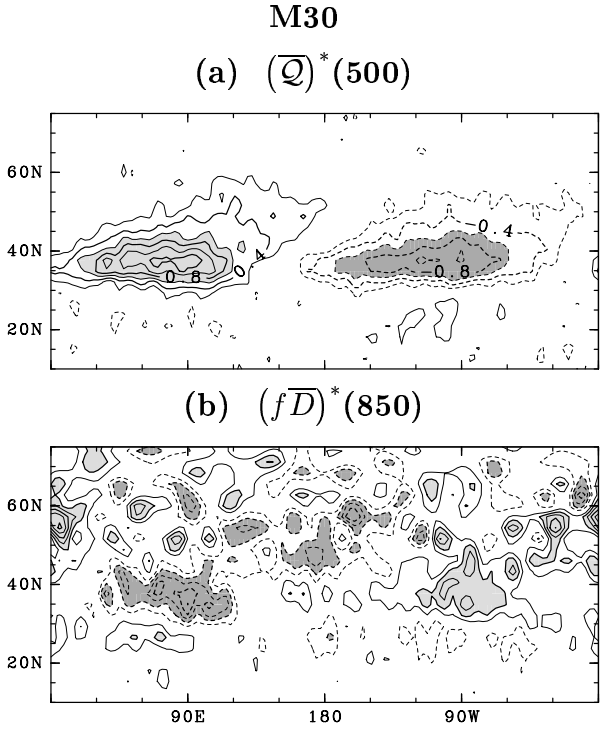
M30
(a) $(\overline{\mathcal{Q}})^*$(500)
60N
40N
20N
0.4
0.8
0.8
(b) $(f\overline{D})^*$(850)
60N
40N
20N
90E
180
90W

Fig. 12.

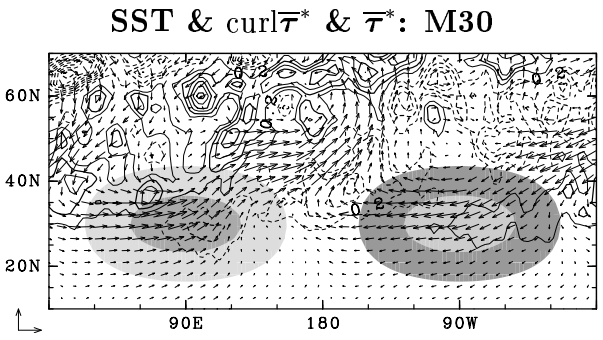
SST & curl$\overline{\tau}^*$ & $\overline{\tau}^*$: M30
60N
40N
20N
90E
180
90W

Fig. 13.

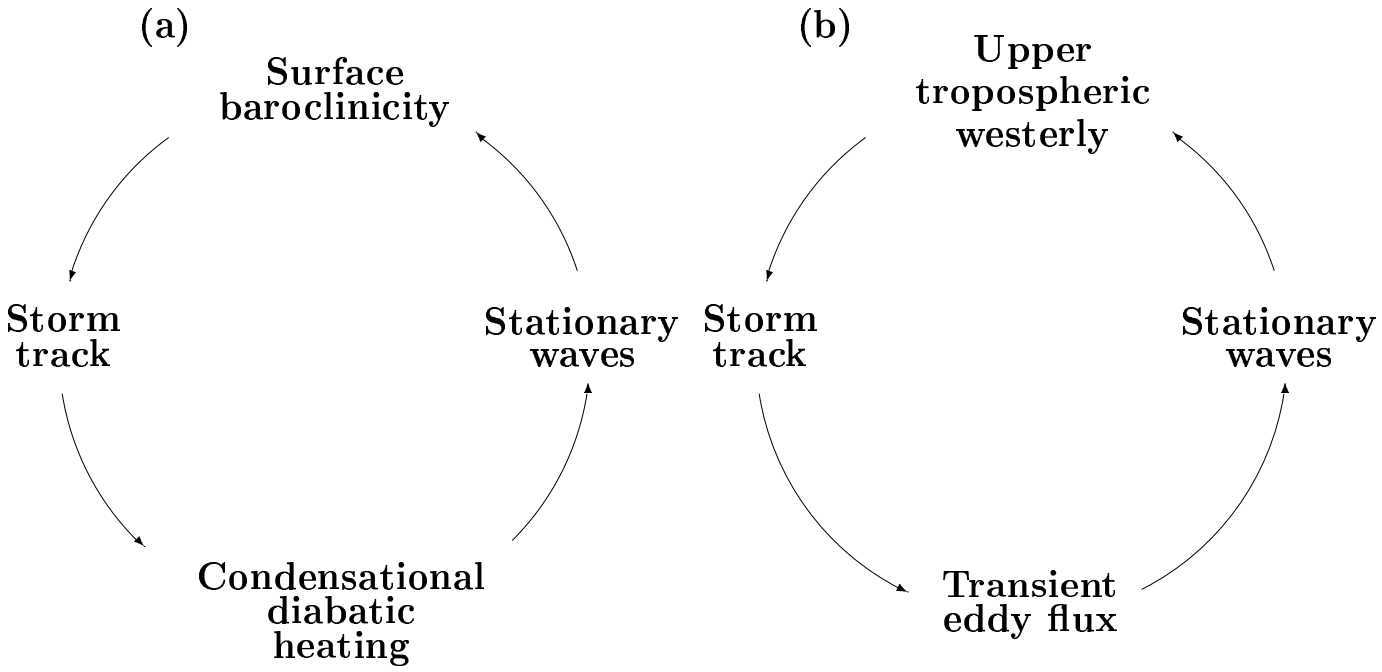
(a)
Surface baroclinicity
Storm track
Stationary waves
Condensational diabatic heating
(b)
Upper tropospheric westerly
Storm track
Stationary waves
Transient eddy flux

Fig. 14.

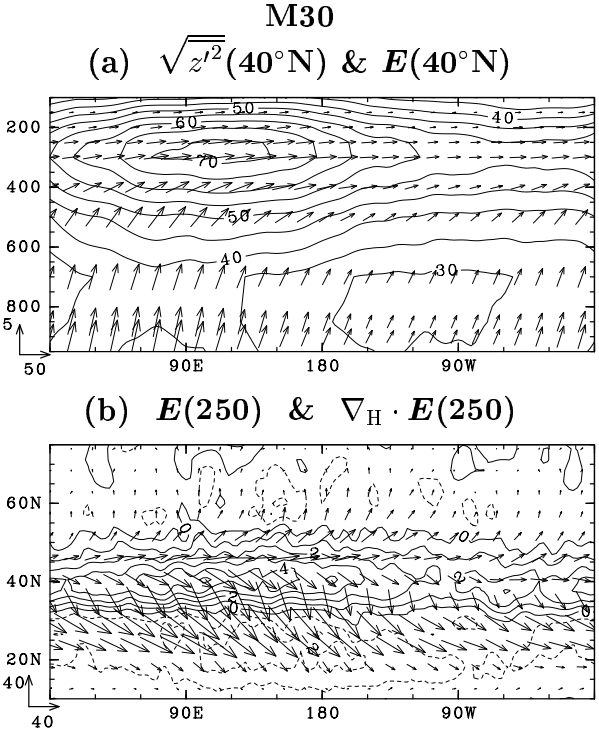
M30
(a) $\sqrt{\overline{z'^2}}(40°\mathrm{N})$ & $\boldsymbol{E}(40°\mathrm{N})$
200
400
600
800
50
60
70
50
40
30
5
50
90E
180
90W
(b) $\boldsymbol{E}(250)$ & $\nabla_{\mathrm{H}} \cdot \boldsymbol{E}(250)$
60N
40N
20N
40
0
2
4
6
8
10
40
90E
180
90W

Fig. B1.